



LAWRENCE  
LIVERMORE  
NATIONAL  
LABORATORY

# Process-Oriented MJO Simulation Diagnostic: Moisture Sensitivity of Simulated Convection

D. Kim, P. Xavier, E. Maloney, M. Wheeler, D. Waliser,  
K. Sperber, H. Hendon, C. Zhang, R. Neale, Y. Hwang,  
H. Liu

May 8, 2013

Journal of Climate

## **Disclaimer**

---

This document was prepared as an account of work sponsored by an agency of the United States government. Neither the United States government nor Lawrence Livermore National Security, LLC, nor any of their employees makes any warranty, expressed or implied, or assumes any legal liability or responsibility for the accuracy, completeness, or usefulness of any information, apparatus, product, or process disclosed, or represents that its use would not infringe privately owned rights. Reference herein to any specific commercial product, process, or service by trade name, trademark, manufacturer, or otherwise does not necessarily constitute or imply its endorsement, recommendation, or favoring by the United States government or Lawrence Livermore National Security, LLC. The views and opinions of authors expressed herein do not necessarily state or reflect those of the United States government or Lawrence Livermore National Security, LLC, and shall not be used for advertising or product endorsement purposes.

Process-oriented MJO Simulation Diagnostic:  
Moisture Sensitivity of Simulated Convection

Daehyun Kim<sup>1†</sup>, Prince Xavier<sup>2</sup>, Eric Maloney<sup>3</sup>, Matthew Wheeler<sup>4</sup>,  
Duane Waliser<sup>5</sup>, Kenneth Sperber<sup>6</sup>, Harry Hendon<sup>4</sup>, Chidong Zhang<sup>7</sup>,  
Richard Neale<sup>8</sup>, Yen-Ting Hwang<sup>9@</sup>, and Haibo Liu<sup>1</sup>  
on behalf of the WMO WGNE MJO Task Force

<sup>1</sup>Lamont-Doherty Earth Observatory, Columbia University, Palisades, New York

<sup>2</sup>Met Office Hadley Centre, Exeter, United Kingdom

<sup>3</sup>Department of Atmospheric Science, Colorado State University, Fort Collins, Colorado

<sup>4</sup>Centre for Australian Weather and Climate Research, Melbourne, Australia

<sup>5</sup>Jet Propulsion Laboratory, California Institute of Technology, Pasadena, California

<sup>6</sup>Lawrence Livermore National Laboratory, PCMDI, Livermore, California

<sup>7</sup>Rosenstiel School of Marine and Atmospheric Science, Miami, Florida

<sup>8</sup>National Center for Atmospheric Research, Boulder, Colorado

<sup>9</sup>Department of Atmospheric Sciences, University of Washington, Seattle

Submitted to Journal of Climate / August 2013

Revised / February 2014

Revised / March 2014

\*Corresponding author address: Daehyun Kim, Lamont-Doherty Earth Observatory, Columbia University, Palisades, NY. E-mail: [dkim@ldeo.columbia.edu](mailto:dkim@ldeo.columbia.edu)

<sup>†</sup>Current affiliation: Department of Atmospheric Sciences, University of Washington, Seattle, WA. E-mail: [daehyun@uw.edu](mailto:daehyun@uw.edu)

<sup>@</sup>Current affiliation: Climate, Atmospheric Science, and Physical Oceanography, Scripps Institute of Oceanography, UC San Diego, La Jolla, California

## Abstract

Process-oriented diagnostics for Madden-Julian oscillation (MJO) simulations are being developed to facilitate improvements in the representation of the MJO in weather and climate models. These process-oriented diagnostics are intended to provide insights into how parameterizations of physical processes in climate models should be improved for a better MJO simulation. In this paper, we propose one such process-oriented diagnostic, which is designed to represent sensitivity of simulated convection to environmental moisture: composites of relative humidity (RH) profile based on precipitation percentiles.

The ability of the RH composite diagnostic to represent the diversity of MJO simulation skill is demonstrated using a group of climate model simulations participating in the Coupled Model Intercomparison Project Phase 3 (CMIP3) and CMIP5. A set of scalar process metrics that captures the key physical attributes of the RH diagnostic is derived and their statistical relationship with indices that quantify the fidelity of the MJO simulation is tested. We find that a process metric that represents the amount of lower-tropospheric humidity increase required for a transition from weak to strong rain regimes has a robust statistical relationship with MJO simulation skill. Our results suggest that moisture sensitivity of convection is closely related to a GCM's ability to simulate the MJO.

## 1. Introduction

The Madden-Julian oscillation (MJO, Madden and Julian 1972) is the dominant mode of intraseasonal variability of the tropics, characterized by planetary spatial scale, a 30-60 day period, and eastward propagation. The MJO interacts with weather and climate phenomena globally (e.g. see reviews in Lau and Waliser, 2011; Zhang 2013). For example, it affects mid-latitude extreme weather events (e.g. Jones 2000), modulates tropical cyclone activity over almost all basins (e.g. Maloney and Hartmann 2000), influences active and break periods of the monsoons globally (e.g. Wheeler and McBride 2005), and triggers and/or terminates some El-Nino events (e.g. Takayabu et al. 1999). Considering its significant impact on high-impact weather and climate phenomena, an appropriate representation of the MJO in climate models seems necessary for an accurate estimate of future changes of those phenomena.

Historically, since the first diagnosis of intraseasonal variability simulated in the models from the Atmospheric Model Intercomparison Project (Slingo et al. 1996), the representation of the MJO in climate models has generally remained unsatisfactory (Waliser et al. 2003; Sperber et al. 2005, 2011; Lin et al. 2006; Kim et al. 2009; Hung et al. 2013). Lin et al. (2006) showed that only 2 among 14 models in the Coupled Model Intercomparison Project-3 (CMIP3) had MJO variance comparable to observations, with even those lacking realism in many other MJO characteristics. Although the models

participating in CMIP5 simulate stronger MJO variance than that of CMIP3 models, the improvement is incremental at best (Hung et al. 2013).

Meanwhile, previous work has shown that the representation of the MJO in GCMs can be improved by changing specific aspects of their cumulus parameterization schemes. Changes that inhibit deep cumulus convection appear to be particularly effective in improving MJO activity (Tokio et al. 1988; Wang and Schlesinger 1999; Maloney and Hartmann 2001; Lee et al. 2003; Zhang and Mu 2005; Lin et al. 2008; Kim and Kang 2012; Kim et al. 2012). Unfortunately, there is an apparent conflict between our ability to improve the MJO simulation while maintaining a realistic basic state. For example, Kim et al. (2011a) showed that mean precipitation over the warmest oceanic areas, which are the north and south western Pacific during boreal summer and winter, respectively, becomes excessive and therefore worsens the mean state as a result of the same parameterization changes that strengthen the MJO in a number of different models. This suggests that those changes in parameterization that benefit the MJO simulation may have been rejected because of higher priority being placed on the mean state simulation compared to simulation of the MJO.

Ideally, a better parameterization must help improve both the mean state and the MJO. Toward this goal, it would be helpful if we have a diagnostic that fulfills all of the following conditions:

- i) the diagnostic can be constructed from currently available observations;

90           ii) the diagnostic is related to certain characteristics of unresolved-scale processes  
91           (i.e. parameterizations) in GCMs;  
92           iii) the diagnostic represents certain features of resolved-scale processes that are  
93           important in the MJO dynamics.

94           If a diagnostic satisfies the first and second conditions, it can provide insight into  
95   how parameterizations should be improved to make model behavior similar to that  
96   diagnosed from observations. If that diagnostic also fulfills the third condition, it will be  
97   a useful tool that could help improve an MJO simulation for the correct physical reason.  
98   Although we expect the mean state will be improved if we improve the MJO simulation  
99   for the right physical reason, it is also possible that other processes may be missing or  
100   misrepresented that prevent a better MJO and realistic mean state at the same time. The  
101   international MJO Task Force<sup>1</sup> has made efforts to develop diagnostics that fulfills the  
102   three conditions listed above – process-oriented MJO simulation diagnostics, with the  
103   overall goal of facilitating improvements in the representation of the MJO in weather  
104   and climate models (Wheeler and Maloney 2013).

105           In this paper, we present one process-oriented MJO simulation diagnostic, which  
106   is designed to better understand the relationship between moisture and convection in

---

<sup>1</sup> The international MJO Task Force had been under World Weather Research Program (WWRP)-The Observing System Research and Predictability Experiment (THORPEX)/World Climate Research Program (WCRP) Year of Tropical Convection (YOTC) during 2010-2012, and is currently under World Meteorological Organization (WMO) Working Group on Numerical Experimentation (WGNE) since January 2013.

the tropical atmosphere, with a particular focus on the lower-tropospheric relative humidity (RH). We base the diagnostic on lower-tropospheric RH over the tropical Indian Ocean that is binned by precipitation percentiles (hereafter, RH Composite based on Precipitation, RHCP).

Similar diagnostics to the RHCP diagnostic used here have been previously used to assess simulations of the MJO in different models (Thayer-Calder and Randall 2009; Zhu et al. 2009; Kim et al. 2009; Del Genio et al. 2012). Although these studies showed the usefulness of tropospheric humidity diagnostics to qualitatively distinguish relatively better MJO models from relatively worse ones, these diagnostics have previously been applied to only a limited number of models. Also, more importantly, the critical aspects and features of the tropospheric humidity distribution and its variability required for an improved simulation of the MJO have not been quantified. To demonstrate the general utility of our RHCP diagnostic, we use multi-model simulation data in the CMIP3 and CMIP5 archives. To identify the key features of the RHCP diagnostic that are related to the simulation capability of the MJO, we derive metrics from the diagnostic and test their statistical relationship with some standard measures of the fidelity of the simulated MJO. Note that although the focus here is on climate models, our findings are equally relevant to weather forecast models.

This paper is organized as follows. Section 2 describes model simulations and observations used, as well as the metrics for MJO simulation fidelity. The way to build



up the RHCP diagnostic will be explained in detail in Section 3. The relationship between the metrics derived from the RHCP diagnostic and the fidelity of the simulated MJO are investigated in Section 4. The summary and conclusions are given in Section 5.

## **2. Data**

### **a) Model simulations**

We use simulation data from a subset of coupled ocean-atmosphere models participating in CMIP3 and CMIP5. Table 1 contains a list of the models used in this study with their convection schemes and horizontal resolutions of their atmospheric component model. Readers are referred to Meehl et al. (2007) and Taylor et al. (2012) for more detailed descriptions of the CMIP3 and CMIP5 archives. Note that the selection of models was based on data availability. For each model, daily-averaged precipitation and outgoing longwave radiation (OLR) during a 20-year period from the 20<sup>th</sup> century simulations was obtained from the archives. For tropospheric RH, we downloaded only a 3-year period of daily data because of limited data storage capacity. Therefore, the measures of MJO simulation fidelity are derived using 20 years of data, while the RHCP diagnostic and the metrics from it are constructed using 3-year data. This inconsistency in data period could affect the results presented here, but evidence indicates that the effect is negligible because the observed RHCP diagnostic derived from 20 years of data

is nearly identical to that from 3 years (not shown). For CMIP3 models, RH was calculated using temperature and specific humidity because RH was not available in the archive. In the case of CMIP5 models, RH was downloaded directly from the archive. The daily averaged RH profiles over the equatorial Indian Ocean (10°S-10°N, 60-90°E) are used to construct the RHCP diagnostic. Because different models have different numbers of vertical levels, we chose four pressure levels that are common to all models used: 1000, 850, 700, and 500 hPa. Among these levels, 850 and 700 hPa are used for the RHCP diagnostic of CMIP3 and CMIP5 models. The reason for excluding 1000 and 500 hPa is given in the following sections.

#### b) Observations and reanalysis

Three precipitation estimates are used to represent the uncertainty in the observations. Version 1.1 of the Global Precipitation Climatology Project (GPCP, Huffman et al. 2001) and the Tropical Rainfall Measuring Mission (TRMM, Huffman et al. 2007) 3B42 version 6 daily-averaged data are used as observational estimates of precipitation. We also use daily-averaged precipitation from the European Centre for Medium-Range Weather Forecasts (ECMWF) ReAnalysis-Interim (ERA-I; Dee et al. 2011). We expect GPCP and TRMM precipitation to be better estimates of observations than ERA-I precipitation, because the reanalysis precipitation product is model-dependent. Nonetheless, ERA-I precipitation is also used in this study. This is because it

was suggested that the satellite measurements used in this study lack capability of observing light rain events (Behrangi et al. 2012), and because the ERA-I precipitation is more physically consistent with one of the RH data used. Daily averaged RH profiles were obtained from two reanalysis products: ERA-I and NASA's Modern-Era Retrospective Analysis for Research and Applications (MERRA, Rienecker et al. 2011). RH from MERRA is used only when we explore the uncertainty in the RHCP diagnostic originated from the source of RH data (Figure 3). All simulations and observations described in this section were regridded into a  $2.5^{\circ} \times 2.5^{\circ}$  grid using a bilinear interpolation scheme before any calculations.

#### c) Fidelity of the MJO simulations

The fidelity of the MJO simulation needs to be quantified in order to make reliable inferences about relationships between the sensitivity of simulated convection to tropospheric humidity and the capability of a model to simulate the MJO. Effective metrics for the latter are needed. Because development of a method that quantifies the quality of MJO simulations in an objective manner is still the area of active research (Crueger et al. 2013), we choose three methods to reduce a possible bias caused from using only one metric.

One simple measure of the MJO is based on the space-time power spectrum of equatorial rainfall (or zonal wind). The ratio of eastward to westward power (E/W ratio)

at MJO time and space scales (zonal wavenumbers 1-3 and periods 30-60 days) reveals the prominence of the eastward propagating intraseasonal variability relative to its westward counterpart (e.g. Zhang and Hendon 1996; Lin et al. 2006; Kim et al. 2009) and is a useful indicator of how prominent the MJO is relative to the background variability. Another measure of MJO activity is the eastward power summed over eastward wavenumbers 1-3 and periods 30-60 days. We refer to this as “East” power. The use of East power alone as a metric for MJO simulation fidelity could be inappropriate if it is unrelated with its westward counterpart (West power). Then model A, which has a smaller E/W ratio than that of model B, could have a greater East power than that of model B. This is usually not the case within the group of models we use, however, as a strong linear relationship between East and West power exists<sup>2</sup>. This allows the use of East power as an index that gives a direct indication as to whether the level of eastward power is realistic. The third measure of MJO fidelity is  $R_{\max}$ , that was recently proposed by Sperber and Kim (2012).  $R_{\max}$  is the maximum correlation between the two time series obtained by projecting model OLR anomalies onto the leading pair of empirical orthogonal functions (EOFs) of observed OLR that capture the MJO. The MJO is deemed well simulated if the correlation between the two leading PCs is strong at a lead-time of about 10-15 days, thereby demonstrating coherent eastward propagation with appropriate spatio-temporal structure.

---

<sup>2</sup> Correlation coefficient between “East” and “West” is about 0.68, which is statistically significant at 95% confidence level.

These measures of MJO fidelity are developed using 20-years (1979-1998) of daily precipitation and OLR data from observations and from the model simulations. The wavenumber-frequency spectra, which the E/W ratio and East power measures of MJO activity are based on, are derived from 10°S-10°N averaged precipitation using the Fast Fourier Transforms applied to 19 segments that are 180 days long (i.e. 19 boreal winters during November-April). For  $R_{\max}$ , the EOF was performed over an extended Indo-Pacific warm pool area (45-240°E, 20°S-20°N) using OLR data during boreal winter (November-April). The values of these three measures from all of the models and the observations are presented in Table 2. In terms of  $R_{\max}$ , no model simulates an MJO stronger than the observed one. Regarding the E/W ratio and East, however, there are models whose MJO is stronger than the observed MJO. For example, cnrm\_cm3 and CNRM-CM5 exhibit the E/W ratio values (5.91 and 4.95, respectively) that are much higher than that of observations (2.09-2.73), and than that of other models. Table 3 provides inter-correlation coefficients between the three measures of MJO fidelity. The correlation coefficients are all positive and statistically significant at the 95% confidence level, indicating they are consistent measures of the MJO simulation fidelity.

### 3. RHCP diagnostic

In this section, we generate the RHCP diagnostic and derive a set of metrics from it. The physical insights from the diagnostic and a brief summary of previous usage of the diagnostic are also given.

#### a) Construction of the RHCP diagnostic

The main purpose of the RHCP diagnostic is to present RH profiles for different regimes that are distinguished from each other by the strength of precipitation. In this study, instead of absolute values of precipitation that has been used in other studies (Thayer-Calder and Randall 2009; Kim et al. 2009; Del Genio et al. 2012), we use precipitation percentiles to make this distinction. Precipitation itself is useful when analyzing a small set of models, but it could be problematic when applied to a large group of models. This is because the statistics of precipitation vary widely between models (Figure 1 and 2). Our calculation of percentiles includes the zero precipitation rate. In fact, in GPCP and TRMM, zero precipitation occupies the lowest 60 and 55 percentiles, respectively, meaning that 60% and 55% of the time there is no rain in GPCP and TRMM (Figure 1). When more than one percentile is occupied with zero values, it is impossible to distinguish RH profiles between those percentiles. Therefore, if this is the case, we make an average of RH profiles over all zero values and assign the mean value to all percentiles filled with zero precipitation values. This is why in Figures 4 and 5 TRMM and GPCP show the same RH value for the lowest 55 and 60 percentiles, respectively.

Figure 1 and 2 display precipitation values of lower 70 and upper 30 precipitation percentiles, respectively. There is a considerable spread among models in almost all percentiles. For example, the top precipitation intensity at the 100<sup>th</sup> percentile (upper 1%) is lower than 30 mm day<sup>-1</sup> in giss\_aom, iap\_fgoals1\_0\_g, and inmcm3\_0, while it is greater than 60 mm day<sup>-1</sup> in cccma\_3\_1\_t63, cnrm\_cm3, and ingv\_echam4. This indicates that the same precipitation rate would correspond to a different percentile in different simulations. Thus, using precipitation percentiles alleviates the influence of systematic discrepancies in the precipitation intensity among the models.

#### b) Physical insights

Figure 3 presents the RHCP diagnostic, which shows the averaged RH profile plotted as a function of precipitation percentiles, constructed using observations and reanalysis data over the central equatorial Indian Ocean (10°S-10°N, 60-90°E). Three different precipitation datasets and two different RH data are used to demonstrate uncertainties in this diagnostic. The lack of ability in two out of three precipitation products (GPCP and TRMM) to distinguish lower percentiles from each other (Fig. 1) inhibited us from estimating the observational uncertainty for the 1<sup>st</sup>-60<sup>th</sup> percentiles.

From Figure 3a-e, which will be regarded as observations in this study, aspects of the large-scale modulation of tropical convection can be seen. For example, strongest rain events (e.g. 100<sup>th</sup> percentile), which presumably are associated with strong deep

convection, occur only when the column is nearly saturated in a very deep layer (up to 200 hPa). When the precipitation rate falls below the 70<sup>th</sup> percentile, high RH (> 85%) is mostly confined to a shallow layer near the surface (1000-900 hPa). The difference between weak- and strong-precipitation regimes suggests that during the transition between the two regimes, the lower troposphere above the boundary layer (850-500 hPa) experiences a significant moistening. Similar interpretation of the RHCP diagnostic (with slight variations) has been provided by earlier studies (e.g., Zhu et al. 2009).

Although the broad features of the RHCP diagnostic described above are not sensitive to the precipitation and RH data used, some details are. In particular, the gradient in ERA-I RH between weak and strong rain regimes is much greater when GPCP precipitation is used, compared to that constructed using ERA-I precipitation. Also, when MERRA RH is used instead of ERA-I RH, the depth of humid layer near the surface becomes shallower, while RH near the 600 hPa becomes greater. Figure 3e displays the root mean squared difference between the five results divided by the average of them, which is an estimate of observational uncertainty. For the 80<sup>th</sup> or higher percentile, the standard deviation is smaller than 10% of the average, while it reaches 15-20% of the average at near 500 hPa for the 60<sup>th</sup>-65<sup>th</sup> percentiles.

In short, the RHCP diagnostic represents physical aspects of the moisture-convection relationship over the central equatorial Indian Ocean, and those features are not sensitive to the data used to construct the diagnostic.



c) Relevant MJO dynamics

The key feature in the RHCP diagnostic concerning the relationship between tropical convection and environmental moisture is the tight coupling between them. The strong coupling between tropical convection and lower-tropospheric moisture has been shown to be an intrinsic characteristic of the tropical atmosphere (Bretherton et al. 2004; Holloway and Neelin 2009). Furthermore, Yasunaga and Mapes (2012) showed that the MJO is distinguished from other convectively coupled equatorial waves by the strong coupling between precipitable water and precipitation (see their Fig. 4). This observational evidence suggests that the tight coupling between moisture and convection should be included in theories of the MJO.

Moisture-convection coupling is a crucial ingredient in some theoretical considerations on the dynamics of the MJO (Blade and Hartmann 1993; Raymond 2001; Bony and Emanuel 2005; Sobel and Maloney 2012, 2013). In these views, enhanced convection associated with the MJO is strongly tied to the positive moisture anomaly, and the growth/decay and propagation of the MJO can be explained by the processes regulating the moisture anomaly. In this case, growth/decay of the MJO is controlled by the physical processes responsible for supporting/reducing moisture anomalies in regions of enhanced convection, and propagation is regulated by the processes responsible for moistening to the east of the convecting region and drying to the west.

305 This 'discharge-recharge' (Blade and Hartmann 1993) or 'moisture mode' (Raymond  
306 2001) view has been supported by observations (e.g. Kemball-Cook and Weare 2001;  
307 Yasunaga and Mapes 2012), reanalysis (Sperber 2003) and modeling studies (e.g.  
308 Sperber et al. 2005; Thayer-Calder and Randall 2009; Zhu et al. 2009, Maloney et al.  
309 2010).

310 In these views of MJO dynamics, it is argued that the time scale required for the  
311 atmosphere to build-up lower-tropospheric moisture and to discharge it determines the  
312 period of the intraseasonal oscillation. A particularly critical physical process is the  
313 gradual accumulation of moisture during the recharge period, which accompanies  
314 deepening and strengthening of the cumulus clouds and takes 15-30 days to transition  
315 from a dry, non-precipitating state to a strongly convecting state. During the recharging  
316 period, strong convection, which consumes the accumulated moisture, should not be  
317 prevalent. This time scale of the recharge process determines the period of MJO, which  
318 is 30-60 days. Also, the recharge preferentially occurs to the east of the developing  
319 convective envelope, thus driving the eastward propagation. Therefore, for a climate  
320 model, an appropriate simulation of the sensitivity of cumulus convection to  
321 environmental humidity would be a necessary condition for a reasonable MJO  
322 simulation.

323

324 d) Previous usage

Moisture diagnostics related to our RHCP diagnostic have been used to distinguish a GCM with a relatively good MJO from a GCM with a relatively poor one in Thayer-Calder and Randall (2009), Zhu et al. (2009), Kim et al. (2009), Kim et al. (2011), and Del Genio et al. (2012). In Kim et al. (2009) and Xavier (2012), the moisture diagnostic was applied to a set of models that exhibited a range of abilities to simulate the MJO. The findings in these studies support the argument that if a model better represents the relationships between the rainfall rate and environmental humidity as depicted in the RHCP diagnostic, the model tends to simulate a better MJO. A typical symptom of relatively poor MJO simulations in these studies is that they simulate too-strong rainfall rates for dry lower-tropospheric RH, meaning they lack the appropriate sensitivity to environmental moisture.

The lack of sensitivity of the parameterized convection to environmental moisture was reported in Derbyshire et al. (2004) as an issue common to a number of models. This lack of sensitivity may result in the poor simulation of the MJO in many models, in which the effect of a cumulus ensemble on the large-scale environment is represented with parameterization schemes. If a strong relationship between the sensitivity of convection to environmental moisture and the fidelity of MJO simulations is found, we could have more confidence in this argument. To investigate this further, we will derive some quantifiable metrics of the moisture-rainfall sensitivity depicted by

the RHCP diagnostic and apply them to a set of models that exhibit a wide range of capabilities to simulate the MJO.

#### e) Derivation of moisture sensitivity metrics

In order to derive quantifiable metrics from the RHCP diagnostic, we constructed the RHCP diagnostic using model simulation data. We present in Figures 4 and 5 the RHCP diagnostic at 850 and 700 hPa, respectively, since as discussed in Section 3b most pronounced moistening occurs above the boundary layer in the transition between the weak and strong precipitation regimes. The model results are compared to those from the ERA-I RH and the three precipitation products.

In Figures 4 and 5 the lower-tropospheric RH increases with precipitation percentile in all models and observations as expected, although considerable spread exists among models for all percentiles. For example, in bccr\_cm2\_0, cnrm\_cm3, and MRI-CGCM3, RH in the lower troposphere is greater than 90% for the upper 10 precipitation percentiles, while the lower-tropospheric RH hardly exceeds 80% in inmcm3\_0, mri\_cgcm2\_3\_2a, and CanESM2. This suggests that the former group of models requires a moister environment than the latter group to produce relatively high rainfall rates. The difference of lower-tropospheric RH between the strong and weak rain regimes also shows variability among simulations. A greater difference suggests a more sensitive convection response to lower-tropospheric RH. In this regard, ERA-I

exhibits RH for the top (100<sup>th</sup>) percentile that is about 45% greater than that of the bottom (1<sup>st</sup>) percentile at 850 hPa (Figure 4). This difference is greater at 700hPa, and is about 50% (Figure 5). Models show a wide range of RH differences between the top and bottom percentiles. For example, at 700hPa, MRI-CGCM3 shows a RH increase of about 65%, while FGOALS-s2 experiences about 40% increase of RH (Figure 5).

These results suggest that both the lower-tropospheric RH in the strong rain regime, and the difference of lower-tropospheric RH between the strong and weak rain regime can be a measure of the moisture sensitivity exhibited by model convection, and will be used as metric in the following. The former can be represented as an average of lower-tropospheric RH for the upper X percent of rain events ( $\overline{RH}^{upper\ X\%}$ ), while the latter can be the difference between  $\overline{RH}^{upper\ X\%}$  and  $\overline{RH}^{lower\ Y\%}$ , where  $\overline{RH}^{lower\ Y\%}$  is an average of lower-tropospheric RH for the lower Y percent of rain rates, as illustrated in the lower part of Figure 4a. The latter moisture sensitivity metric ( $\overline{RH}^{upper\ X\%} - \overline{RH}^{lower\ Y\%}$ ) represents the gross gradient of mean RH between the weak and strong rain regimes. In our analysis, lower-tropospheric RH will be measured by a simple average of RH at 850 and 700 hPa levels. The 500 hPa level is excluded because inclusion of the level degrades the relationship between the moisture sensitivity metric and the MJO simulation fidelity metrics (not shown). By choosing levels in the lower-tropospheric layer (850 and 700 hPa) that exclude the planetary boundary layer, we aim to capture only the effects of environmental air on cumulus convection through entrainment to

cumulus updrafts, and excluding the effects from the planetary boundary layer moisture (i.e. increasing or decreasing convective available potential energy). Therefore, RH at 1000 hPa level is not used in the calculations below. Properly representing the effects of entrainment in the lower free troposphere has been shown to be critical for producing realistic convective sensitivity to environmental humidity in models (e.g. Sahany et al. 2012).

#### **4. Statistical relationship between MJO simulation fidelity and moisture-convection coupling metrics**

We now explore the statistical relationship between the moisture sensitivity metrics derived from the RHCP diagnostic and the measures of the MJO simulation fidelity. Our examination revealed that the  $\overline{RH}^{upper\ X\%} - \overline{RH}^{lower\ Y\%}$  metric has a stronger relationship with the MJO simulation fidelity metrics than  $\overline{RH}^{upper\ X\%}$  regardless of Y (not shown). This implies that in a GCM that simulates a relatively skillful MJO, the mean RH of the strong rain events is relatively higher than that of the weak rain events. Therefore we present later only the results based on  $\overline{RH}^{upper\ X\%} - \overline{RH}^{lower\ Y\%}$ .

Figure 6 presents the linear relationship (i.e. correlation coefficient) between  $\overline{RH}^{upper\ X\%} - \overline{RH}^{lower\ Y\%}$  and three measures of the MJO simulation fidelity as a function

of X (x-axis) and Y (y-axis). Only model data is used in the calculation of the correlation coefficients. Although the dependence of the linear relationship on X and Y varies with the measure of the MJO simulation fidelity used, the linear relationship is statistically significant at 95% confidence level, which is 0.32<sup>3</sup>, in a wide area for all MJO simulation fidelity metrics used. Also, Figure 6 shows that the strongest relationship is found when the E/W power ratio is used as a measure of the MJO skill. An average of the linear relationship with the three MJO simulation fidelity metrics (Figure 6d) suggests that the average correlation coefficient is greater than 0.7 if we choose X between 2 and 20, and Y between 15 and 30, respectively.

As seen in Figure 7, when X is fixed at 10, the averaged correlation coefficient is higher with Y near 20 (Figure 7a), and when Y is fixed at 20, the averaged linear relationship maximizes with X around 10 (Figure 7c). In both cases, the peak is broad enough to conclude that the averaged linear relationship is not sensitive to a specific choice of X and Y. With X=10 and Y=20, the moisture sensitivity metric ( $\overline{RH}^{upper\ 10\%} - \overline{RH}^{lower\ 20\%}$ ) can explain on average 50% of inter-model variability in their MJO simulation fidelity, although its skill varies with the MJO simulation fidelity metrics (Figure 7b,d).

---

<sup>3</sup> Note that we count all models when estimating the degree of freedom (=28). The degree of freedom could be lower than the number of models we are using, as there are different versions of same models: gfdl\_cm2\_0/gfdl\_cm2\_1, CMCC-CM/CMCC-CMS, MIROC4h/MIROC-ESM/MIROC-ESM-CHEM, and MPI-ESM-LR/MPI-ESM-CHEM. If we consider these groups of models as one model then the degree of freedom drops to 23, and the 95% confidence level increases to 0.35.

As seen in Figure 8 for  $X=10$  and  $Y=20$ , the E/W and East relationship to  $\overline{RH}^{upper\ 10\%} - \overline{RH}^{lower\ 20\%}$  explains about 56% of inter-model variability, while for  $R_{max}$  the explained variance is 48% (Figure 8). Actually,  $\overline{RH}^{upper\ 10\%} - \overline{RH}^{lower\ 20\%}$  explains about 65% of inter-model variability in E/W when we remove two CNRM models whose E/Ws are outliers (Table 2).

Our results imply that models simulate a stronger MJO if they require a greater difference in lower-tropospheric RH between strong and weak rain percentiles. In other words, in the models that simulate stronger MJO activity, convection is more sensitive to lower-tropospheric humidity. This is consistent with the results of Hannah and Maloney (2011) and Kim et al. (2012) in which strengthening of the moisture-convection relationship caused a stronger MJO in different GCMs. Kim et al. (2012) increased the fractional entrainment rate and re-evaporation of convective condensates in the convection scheme of the National Aeronautics and Space Administration Goddard Institute for Space Study GCM to make deep convection more sensitive to environmental humidity, which led the GCM to simulate an improved MJO.

In Figure 8, results are also presented for the three observed precipitation products and ERA-I RH data. Note that in all cases we use the  $\overline{RH}^{lower\ 20\%}$  value that is obtained using ERA-I precipitation, while for  $\overline{RH}^{upper\ 10\%}$  their own values are used. This is because, as mentioned earlier, with GPCP and TRMM it is impractical to distinguish the lowest 20% percentiles exclusively from others. Although the



relationship between the moisture sensitivity of convection and the MJO simulation fidelity seems robust within GCMs, the same relationship cannot explain the observations. When compared to observations, models have too strong moisture sensitivity of convection when they represent a skillful MJO, and have too weak MJO when they simulate a reasonable moisture sensitivity of convection. This is especially true when  $R_{\max}$  is used as a MJO simulation fidelity metric (Figure 8c). In other words, GCMs in general underestimate the strength of the MJO for a given moisture sensitivity of convection. This suggests that processes important in MJO simulation other than moisture-convection relationship could be commonly misrepresented in GCMs.

The results in this section show that the amount of moistening required for the transition from weak to strong rain regimes has a robust statistical relationship with the fidelity metrics of the simulated MJOs. In particular, the above results suggest that the RHCP diagnostic could be a useful tool as a process-oriented MJO simulation diagnostic, and that  $\overline{RH}^{upper\ 10\%} - \overline{RH}^{lower\ 20\%}$  could be a useful metric to look at when developing climate models and considering their capability to simulate the MJO.

## 5. Summary and Conclusion

A process-oriented MJO simulation diagnostic based on free tropospheric relative humidity is proposed and tested. The process-oriented MJO simulation diagnostic aims to give physical insight into why a GCM simulates a stronger or weaker

MJO than others (c.f. Wheeler and Maloney 2013). Three aspects are required of such a diagnostic: i) currently available observations can be used to construct it, ii) changes in parameterizations alter its behavior, and iii) it has a tight relationship with the fidelity of the simulated MJO, meaning it has relevance to MJO dynamics, at least in models.

We propose the RH Composite based on Precipitation (RHCP) diagnostic as a process-oriented MJO simulation diagnostic. The RHCP diagnostic is derived by binning RH profiles into precipitation percentiles. When applied to model simulations, it represents the simulated interaction between cumulus convection and environmental humidity, and so is closely related to the moisture sensitivity of deep and shallow cumulus parameterizations in the climate model. It is also relevant to theories of the MJO in which the tight coupling between convection and environmental moisture is a crucial ingredient.

Statistical relationships between a set of moisture sensitivity metrics deduced from the RHCP diagnostic and objective measures of the simulated MJOs are investigated. The moisture sensitivity metrics are developed as the mean lower-tropospheric RH for upper X percent rain events minus that for lower Y percent rain events ( $\overline{RH}^{upper\ X\%} - \overline{RH}^{lower\ Y\%}$ ). Sensitivity of its skill in explaining MJO simulation fidelity to adjustable parameters - X and Y - is also investigated. A robust statistical relationship with the strength of the simulated MJO was found when  $\overline{RH}^{upper\ 10\%} - \overline{RH}^{lower\ 20\%}$  is used as the moisture sensitivity metric. Based on our results, we propose

481  $\overline{RH}^{upper\ 10\%} - \overline{RH}^{lower\ 20\%}$  as a moisture sensitivity metric that can be used to assess  
482 MJO simulations. The robust statistical relationship of  $\overline{RH}^{upper\ 10\%} - \overline{RH}^{lower\ 20\%}$  with  
483 the fidelity of MJO simulation found in this study suggests that a GCM's ability to  
484 simulate the MJO is closely related to the moisture sensitivity of convection simulated  
485 in the GCM. Further studies are required to reveal effects of specific parameterization  
486 changes on the RHCP diagnostic and the moisture sensitivity metric in each model.

487         Observational estimates of  $\overline{RH}^{upper\ 10\%} - \overline{RH}^{lower\ 20\%}$  do not uniformly lie along  
488 the linear relationship derived from GCM simulations. Models require too-strong  
489 moisture sensitivity to produce a reasonable MJO in terms of the MJO simulation  
490 fidelity metrics used, while they show too-weak MJO with reasonable moisture  
491 sensitivity. Although the robust statistical relationship between the moisture sensitivity  
492 metric and the MJO simulation fidelity among GCMs suggests the relevance of the  
493 processes that regulate moisture sensitivity of convection on MJO dynamics in those  
494 GCMs, and probably in nature, the mismatch with observations suggests that there  
495 could be processes other than moisture sensitivity of simulated convection that are  
496 relevant to the MJO dynamics. It is possible that those processes are commonly missing  
497 or misrepresented in models. Longwave cloud radiative feedback could be one such  
498 process. During an active phase of the MJO, an enhanced amount of high cloud reduces  
499 longwave radiative cooling, which means a heating in an anomaly sense. This heating  
500 from cloud-radiation interaction has been suggested as an important destabilization

501 mechanism of the MJO in observational (Lin and Mapes 2004, Ma and Kuang 2011;  
502 Landu and Maloney 2011b; Kim et al. 2014), theoretical (Hu and Randall 1994; 1995;  
503 Raymond 2001; Sobel and Gildor 2003; Sobel and Maloney 2012; 2013), and modeling  
504 studies (Bony and Emanuel 2005; Landu and Maloney 2011a; Kim et al. 2011b;  
505 Anderson and Kuang 2012). Future work should focus on the cloud-radiation  
506 interaction as well as identifying other processes relevant to the MJO dynamics.

507         There are uncertainties in observations. The RH data used in this study is from  
508 reanalysis product, which is a model simulation constrained by observations. Because  
509 observations of RH in areas with strong convection is an extremely difficult task with  
510 current technology, the reanalysis RH in these areas is heavily influenced by model  
511 parameterizations, and therefore could be biased. The two satellite precipitation  
512 products – TRMM 3B42 and GPCP v1.1 use observations of infrared (IR) brightness  
513 temperature to estimate surface rain rate. Behrangi et al. (2012) suggested that IR-based  
514 precipitation products could underestimate the frequency of light rain ( $< 1\text{mm day}^{-1}$ ),  
515 due to the bias in the relationship they are using between IR brightness temperature  
516 and microwave precipitation measurements. We suspect that the lack of weak rain  
517 events in TRMM 3B42 and GPCP v1.1 (Figures 1 and 2), which led us to excluding these  
518 data when estimating the mean lower-tropospheric RH for weak rain regime  
519 ( $\overline{RH}^{lower\ 20\%}$ ), could be due to this weakness of the data. Advances in retrieval  
520 algorithms for lower tropospheric RH and light rain rates, and in data assimilation

schemes used in creating reanalysis products will help to constrain the moisture sensitivity metric with a higher confidence on observations.

## Acknowledgements

This work was conducted under a subproject of the WMO WGNE MJO Task Force. The authors acknowledge stimulating feedback from the entire task force that greatly benefitted this work. We also thank anonymous reviewers for their constructive comments. DK is supported by the NASA grant NNX13AM18G and the Korea Meteorological Administration Research and Development Program under Grant CATER 2013-3142. EDM is supported by Climate and Large-Scale Dynamics Program of the National Science Foundation under Grants ATM-0832868 and AGS-1025584 and the Science and Technology Center for Multi-Scale Modeling of Atmospheric Processes, managed by Colorado State University under Cooperative Agreement No. ATM-0425247. EDM is also supported by Award NA08OAR4320893 and NA12OAR4310077 from the National Oceanic and Atmospheric Administration, U.S. Department of Commerce and NASA Grant # NNX13AQ50G. The ERA-Interim data used in this study have been provided by the ECMWF data server.

Prepared by LLNL under Contract DE-AC52-07NA27344.

539 **References**

- 540 Arakawa, A., and W. H. Schubert, 1974: Interactions of cumulus cloud ensemble with  
541 the large-scale environment. Part I, *J. Atmos. Sci.*, **31**, 671–701.
- 542 Andersen, Joseph Allan, Zhiming Kuang, 2012: Moist Static Energy Budget of MJO-like  
543 Disturbances in the Atmosphere of a Zonally Symmetric Aquaplanet. *J. Climate*,  
544 **25**, 2782–2804.
- 545 Behrangi, A., M. Lebsock, S. Wong, and B. Lambrigtsen, 2012: On the quantification of  
546 oceanic rainfall using spaceborne sensors. *J. Geophys. Res.*, **117**, D20105.
- 547 Betts A.K., 1986: A new convective adjustment scheme. Part I. Observational and  
548 theoretical basis. *Quart. J. Roy. Met. Soc.*, **112**, 677-691.
- 549 Bladé, I., and Hartmann, D. L., 1993: Tropical intraseasonal oscillations in a simple  
550 nonlinear model. *J. Atmos. Sci.*, **50**, 2922-2939.
- 551 Bony, S., and Emanuel, K. A., 2005: On the Role of Moist Processes in Tropical  
552 Intraseasonal Variability: Cloud–Radiation and Moisture–Convection Feedbacks.  
553 *J. Atmos. Sci.*, **62**, 2770–2789.
- 554 Bougeault, P., 1985: A simple parameterization of the large-scale effects of cumulus  
555 convection. *Mon. Wea. Rev.*, **113**, 2108–2121.
- 556 Bretherton, C. S., M. E. Peters, and L. E. Back, 2004: Relationship between water vapor  
557 path and precipitation over the tropical oceans. *J. Climate*, **17**, 1517-1528.

558 CLIVAR MJO Working Group, 2009: MJO Simulation Diagnostics. *J. Climate*, **22**, 3006–  
559 3030. doi: <http://dx.doi.org/10.1175/2008JCLI2731.1>

560 T. Crueger, B. Stevens and R. Brokopf (2013). The Madden-Julian Oscillation in  
561 ECHAM6 and the Introduction of an Objective MJO Metric. *J. Climate*, **26**, 3241–  
562 3257, doi:10.1175/JCLI-D-12-00413.1.

563 Dee, D. P., S. M. Uppala, A. J. Simmons, P. Berrisford, P. Poli, S. Kobayashi, U. Andrae,  
564 M. A. Balmaseda, G. Balsamo, P. Bauer, P. Bechtold, A. C. M. Beljaars, L. van de  
565 Berg, J. Bidlot, N. Bormann, C. Delsol, R. Dragani, M. Fuentes, A. J. Geer, L.  
566 Haimberger, S. B. Healy, H. Hersbach, E. V. Hólm, L. Isaksen, P. Kållberg, M.  
567 Köhler, M. Matricardi, A. P. McNally, B. M. Monge-Sanz, J. J. Morcrette, B. K.  
568 Park, C. Peubey, P. de Rosnay, C. Tavalato, J. N. Thépaut, and F. Vitart, 2011: The  
569 ERA-Interim reanalysis: configuration and performance of the data assimilation  
570 system. *Q. J. R. Meteorol. Soc.*, **137**, 553-597.

571 Del Genio, A.D., and M.-S. Yao, 1993: Efficient cumulus parameterization for long-term  
572 climate studies: The GISS scheme. In *The Representation of Cumulus Convection*  
573 *in Numerical Models*, AMS Meteor. Monograph. K.A. Emanuel, and D.A.  
574 Raymond, Eds., vol. 24, no. 46. American Meteorological Society, 181-184.

575 Del Genio, A. D., Y. Chen, D. Kim, and M.-S. Yao, 2012: The MJO Transition from  
576 Shallow to Deep Convection in CloudSat/CALIPSO Data and GISS GCM  
577 Simulations. *J. Climate*, **25**, 3755-3770.

578 Derbyshire, S., I. Beau, P. Bechtold, J. Y. Grandpeix, J. M. Piriou, J. L. Redelsperger, and  
 579 P. Soares, 2004: Sensitivity of moist convection to environmental humidity. *Q. J.*  
 580 *R. Meteorol. Soc.*, **130**, 3055-3079.

581 Emanuel, K. A., 1991: A scheme for representing cumulus convection in large-scale  
 582 models. *J. Atmos. Sci.*, **48**, 2313–2335.

583 Emori, S., T. Nozawa, A. Numaguti, and I. Uno, 2001: Importance of cumulus  
 584 parameterization for precipitation simulation over East Asia in June. *J. Meteor.*  
 585 *Soc. Japan*, **79**, 939–947.

586 Gregory, D., P. R. Rowntree, 1990: A Mass Flux Convection Scheme with  
 587 Representation of Cloud Ensemble Characteristics and Stability-Dependent  
 588 Closure. *Mon. Wea. Rev.*, **118**, 1483–1506.

589 Hannah, W. M., and E. D. Maloney, 2011: The role of moisture-convection feedbacks in  
 590 simulating the Madden-Julian oscillation. *J. Climate*, **24**, 2754-2770.

591 Huffman, G. J., R. F. Adler, M. Morrissey, D. T. Bolvin, S. Curtis, R. Joyce, B. McGavock,  
 592 and J. Susskind, 2001: Global precipitation at one-degree daily resolution from  
 593 multisatellite observations. *J. Hydrometeor.*, **2**, 36–50.

594 Huffman, G. J., and Coauthors, 2007: The TRMM Multisatellite Precipitation Analysis  
 595 (TMPA): Quasi-Global, Multiyear, Combined-Sensor Precipitation Estimates at  
 596 Fine Scales. *J. Hydrometeor.*, **8**, 38–55.



597 Hung, M-P., J.-L. Lin, W. Wang, D. Kim, T. Shinoda, and S. J. Weaver, 2013: MJO and  
 598 convectively coupled equatorial waves simulated by CMIP5 climate models, *J.*  
 599 *Climate*, 6185-6124.

600 Hu, Q., and D. A. Randall, 1994: Low-Frequency Oscillations in Radiative-Convective  
 601 Systems. *J. Atmos. Sci.*, **51**, 1089-1099.

602 Hu, Q., and D. A. Randall, 1995: Low-Frequency Oscillations in Radiative-Convective  
 603 Systems. Part II: An idealized model. *J. Atmos. Sci.*, **52**, 478-490.

604 Holloway, C. E., and J. D. Neelin, 2009: Moisture vertical structure, column water  
 605 vapor, and tropical deep convection. *J. Atmos. Sci.*, **66**, 1665-1683.

606 Jones, C., 2000: Occurrence of extreme precipitation events in California and  
 607 relationships with the Madden-Julian oscillation. *J. Climate*, **13**, 3576-3587.

608 Kemball-Cook, S. R. and B. C. Weare, 2001: The onset of convection in the Madden-  
 609 Julian oscillation. *J. Climate*, **14**, 780-793.

610 Kim, D., K. Sperber, W. Stern, D. Waliser, I. S. Kang, E. Maloney, W. Wang, K.  
 611 Weickmann, J. Benedict, and M. Khairoutdinov, 2009: Application of MJO  
 612 simulation diagnostics to climate models. *J. Climate*, **22**, 6413-6436.

613 Kim, D., A. H. Sobel, D. Frierson, E. Maloney, and I. S. Kang, 2011a: A systematic  
 614 relationship between intraseasonal variability and mean state bias in AGCM  
 615 simulations. *J. Climate*, **24**, 5506-5520.

616 Kim, D., A. H. Sobel, and I.-S. Kang, 2011b: A Mechanism Denial Study on the Madden-  
617 Julian Oscillation. *J. Adv. Model. Earth Syst.*, **3**, M12007.

618 Kim, D. and I. S. Kang, 2012: A bulk mass flux convection scheme for climate model:  
619 description and moisture sensitivity. *Climate Dynamics*, **38**, 411-429.

620 Kim, D., A. H. Sobel, A. D. Del Genio, Y. Chen, S. J. Camargo, M.-S. Yao, M. Kelley, and  
621 L. Nazarenko, 2012: The Tropical Subseasonal Variability Simulated in the NASA  
622 GISS General Circulation Model. *J. Climate*, **25**, 4641-4659.

623 Kim, D., J.-S. Kug, and A. H. Sobel, 2014: Propagating vs. Non-propagating Madden-  
624 Julian oscillation events. *J. Climate*, **27**, 111-125.

625 Landu, K., and E. D. Maloney, 2011a: Understanding intraseasonal variability in an  
626 aquaplanet GCM. *J. Meteor. Soc. Japan*, **89**, 195-210, doi:10.2151/jmsj.2011-302.

627 Landu, K., and E. D. Maloney, 2011b: The intraseasonal moist static energy budget in  
628 reanalysis data. *J. Geophys. Res.*, **116**, D21117, doi:10.1029/2011JD016031.

629 Lau, W. K., and Waliser, D. E., 2011: Intraseasonal variability in the atmosphere-ocean  
630 climate system. *Springer*, 648pp.

631 Lee, M. I., I. S. Kang, and B. E. Mapes, 2003: Impacts of cumulus convection  
632 parameterization on aqua-planet AGCM Simulations of tropical intraseasonal  
633 variability. *J. Meteorol. Soc. Japan*, **81**, 963-992.

634 Lin, J. L. and B. E. Mapes, 2004a: Radiation budget of the tropical intraseasonal  
635 oscillation. *Journal of the Atmospheric Sciences*, **61**, 2050-2062.

636 Lin, J. L., M. I. Lee, D. Kim, I. S. Kang, and D. M. W. Frierson, 2008: The Impacts of  
 637 Convective Parameterization and Moisture Triggering on AGCM-Simulated  
 638 Convectively Coupled Equatorial Waves. *J. Climate*, **21**, 883-909.

639 Lin, J. L., G. N. Kiladis, B. E. Mapes, K. M. Weickmann, K. R. Sperber, W. Lin, M. C.  
 640 Wheeler, S. D. Schubert, A. Del Genio, L. J. Donner, S. Emori, J. F. Gueremy, F.  
 641 Hourdin, P. J. Rasch, E. Roeckner, and J. F. Scinocca, 2006: Tropical intraseasonal  
 642 variability in 14 IPCC AR4 climate models. Part I: Convective signals. *J. Climate*,  
 643 **19**, 2665-2690.

644 Ma, D. and Z. Kuang, 2011: Modulation of Radiative Heating by the Madden-Julian  
 645 Oscillation and Convectively Coupled Kelvin Waves as Observed by CloudSat,  
 646 *Geophys. Res. Letts.*, **38**, L21813.

647 Madden, R. A. and P. R. Julian, 1972: Description of Global-Scale Circulation Cells in the  
 648 Tropics with a 40-50 Day Period. *J. Atmos. Sci.*, **29**, 1109-1123.

649 Maloney, E. D. and D. L. Hartmann, 2000: Modulation of hurricane activity in the Gulf  
 650 of Mexico by the Madden-Julian oscillation. *Science*, **287**, 2002-2004.

651 — —, 2001: The sensitivity of intraseasonal variability in the NCAR CCM3 to changes in  
 652 convective parameterization. *J. Climate*, **14**, 2015-2034.

653 Maloney, E. D., A. H. Sobel, and W. M. Hannah, 2010: Intraseasonal variability in an  
 654 aquaplanet general circulation model. *J. Adv. Modeling. Earth. Sys*, **2**, Art. #5, 24  
 655 pp.

656 Meehl, G. A., C. Covey, T. Delworth, M. Latif, B. McAvaney, J. F. B. Mitchell, R. J.  
 657 Stouffer, and K. E. Taylor, 2007: The WCRP CMIP3 multi-model dataset: A new  
 658 era in climate change research, *Bull. Amer. Meteor. Soc.*, **88**, 1383-1394.

659 Moorthi, S., and M. J. Suarez, 1992: Relaxed Arakawa-Schubert: A parameterization of  
 660 moist convection for general circulation models. *Mon. Wea. Rev.*, **120**, 978-1002.

661 Neale, R. B., J. H. Richter, and M. Jochum, 2008: The impact of convection on ENSO:  
 662 From a delayed oscillator to a series of events, *J. Climate*, **21**, 5904-5924.

663 Nordeng, T. E., 1994: Extended versions of the convective parameterization scheme at  
 664 ECMWF and their impact on the mean and transient activity of the model in the  
 665 tropics. Technical Memorandum 206, ECMWF, Reading, UK.

666 Pan, D.-M., and D. A. Randall, 1998: A cumulus parameterization with a prognostic  
 667 closure. *Quart. J. Roy. Meteor. Soc.*, **124**, 949-981.

668 Raymond, D. J., 2001: A new model of the Madden-Julian Oscillation, *J. Atmos. Sci.*, **58**,  
 669 2807-2819.

670 Richter, J. H., and P. J. Rasch, 2008: Effects of convective momentum transport on the  
 671 atmospheric circulation in the community atmosphere model, version 3, *J.*  
 672 *Climate*, **21**, 1487-1499.

673 Rienecker, M.M., and coauthors, 2011. MERRA - NASA's Modern-Era Retrospective  
 674 Analysis for Research and Applications. *J. Climate*, **24**, 3624-3648, doi: 10.1175/JCLI-  
 675 D-11-00015.1.

676 Sahany, S., J. D. Neelin, K. Hales, R. B. Neale, 2012: Temperature–Moisture Dependence  
677 of the Deep Convective Transition as a Constraint on Entrainment in Climate  
678 Models. *J. Atmos. Sci.*, **69**, 1340–1358.

679 Slingo, J. M., K. R. Sperber, J. S. Boyle, J. P. Ceron, M. Dix, B. Dugas, W. Ebisuzaki, J.  
680 Fyfe, D. Gregory, J. F. Gueremy, J. Hack, A. Harzallah, P. Inness, A. Kitoh, W. K.  
681 M. Lau, B. McAvaney, R. Madden, A. Matthews, T. N. Palmer, C. K. Park, D.  
682 Randall, and N. Renno, 1996: Intraseasonal oscillations in 15 atmospheric general  
683 circulation models: Results from an AMIP diagnostic subproject. *Climate*  
684 *Dynamics*, **12**, 325-357.

685 Sobel, A. H., and S. Gildor, 2003: A simple time-dependent model of SST hot spots. *J.*  
686 *Climate*, **16**, 3978-3992.

687 Sobel, A. H. and E. D. Maloney, 2012: An idealized semi-empirical framework for  
688 modeling the Madden-Julian oscillation. *J. Atmos. Sci.*, **69**, 1691–1705.

689 Sobel, A. H. and E. D. Maloney, 2013: Moisture modes and the eastward propagation of  
690 the MJO. *J. Atmos. Sci.*, **70**, 187-192.

691 Sperber, K. R., 2003: Propagation and the vertical structure of the Madden-Julian  
692 oscillation. *Mon. Wea. Rev.*, **131**, 3018-3037.

693 Sperber, K. R., S. Gualdi, S. Legutke, and V. Gayler, 2005: The Madden-Julian oscillation  
694 in ECHAM4 coupled and uncoupled general circulation models. *Climate*  
695 *Dynamics*, **25**, 117-140.

696 Sperber, K. R. and D. Kim, 2012: Simplified metrics for the identification of the Madden-  
697 Julian oscillation in models. *Atmos. Sci. Lett.*, **13**, 187-193. doi: 10.1002/asl.378

698 Takayabu, Y. N., T. Iguchi, M. Kachi, A. Shibata, and H. Kanzawa, 1999: Abrupt  
699 termination of the 1997-98 El Nino in response to a Madden-Julian oscillation.  
700 *Nature*, **402**, 279-282.

701 Taylor, K.E., R.J. Stouffer, G.A. Meehl, 2012: An Overview of CMIP5 and the experiment  
702 design. *Bull. Amer. Meteor. Soc.*, **93**, 485-498.

703 Thayer-Calder, K. and D. A. Randall, 2009: The role of convective moistening in the  
704 Madden-Julian oscillation. *J. Atmos. Sci.*, **66**, 3297-3312.

705 Tiedtke, M., 1989: A comprehensive mass flux scheme for cumulus parameterization in  
706 large-scale models. *Mon. Wea. Rev.*, **117**, 1779-1800.

707 Tokioka, T., K. Yamazaki, A. Kitoh, and T. Ose, 1988: The equatorial 30-60 day  
708 oscillation and the Arakawa-Schubert penetrative cumulus parameterization. *J.*  
709 *Meteorol. Soc. Japan*, **66**, 883-901.

710 Waliser, D. E., K. Jin, I. S. Kang, W. F. Stern, S. D. Schubert, M. L. Wu, K. M. Lau, M. I.  
711 Lee, J. Shukla, V. Krishnamurthy, V. Satyan, A. Kitoh, G. A. Meehl, V. Y. Galin, G.  
712 Wu, Y. Liu, and C. K. Park, 2003: AGCM Simulations of Intraseasonal Variability  
713 Associated with the Asian Summer Monsoon. *Climate Dynamics*, **21**, 423-446.

714 Wang, W. and M. E. Schlesinger, 1999: The dependence on convection parameterization  
 715 of the tropical intraseasonal oscillation simulated by the UIUC 11-layer  
 716 atmospheric GCM. *J. Climate*, **12**, 1423-1457.

717 Wheeler, M. C. and J. L. McBride, 2005: Australian-Indonesian monsoon. Intraseasonal  
 718 Variability in the Atmosphere-Ocean Climate System, W. K. M. Lau and D. E.  
 719 Waliser, Eds., Springer, Heidelberg, Germany, 125-173.

720 Wheeler, M. W., E. D. Maloney, and the MJO Task Force, 2013: Madden-Julian  
 721 Oscillation (MJO) Task Force: a joint effort of the climate and weather  
 722 communities. *CLIVAR Exchanges*. No. 61 (Vol 18 No.1).

723 Xavier, P. K., 2012: Intraseasonal convective moistening in CMIP3 models. *J. Climate*, **25**,  
 724 2569-2577.

725 Yasunaga, K., and B. E. Mapes, 2012: Differences between more-divergent vs. more-  
 726 rotational types of Convectively Coupled Equatorial Waves. Part I: Space-Time  
 727 Spectral Analyses. *J. Atmos. Sci.*, **69**, 3–16.

728 Yukimoto, S., H. Yoshimura, M. Hosaka, T. Sakami, H. Tsujino, M. Hirabara, T. Y.  
 729 Tanaka, M. Deushi, A. Obata, H. Nakano, Y. Adachi, E. Shindo, S. Yabu, T. Ose,  
 730 and A. Kitoh, 2011: Meteorological Research Institute Earth System Model  
 731 Version 1 (MRI-ESM1)—Model Description—. Tech. Rep. of MRI, 64, 83 pp.

732 Zhang, C. and Hendon, H. H., 1997: On the propagating and standing components of  
 733 the intraseasonal oscillation in tropical convection. *J. Atmos. Sci.*, **54**, 741-752.

734 Zhang, C., 2005: Madden-Julian Oscillation. *Reviews of Geophysics*, **43**, RG2003,  
735 doi:10.1029/2004RG000158.

736 Zhang, G. J., N. A. McFarlane, 1995: Sensitivity of climate simulations to the  
737 parameterization of cumulus convection in the Canadian Climate Centre general  
738 circulation model. *Atmos. Ocean.*, **33**, 407–446

739 Zhang, G. J. and M. Mu, 2005: Simulation of the Madden-Julian Oscillation in the NCAR  
740 CCM3 Using a Revised Zhang-McFarlane Convection Parameterization Scheme.  
741 *J. Climate*, **18**, 4046-4064.

742 Zhu, H., H. H. Hendon, and C. Jakob, 2009: Convection in a parameterized and  
743 superparamaterized model and its role in the representation of the MJO . *J. Atmos.*  
744 *Sci.*, **66**, 2796-2811.



745    **Table list**

746    Table 1. List of participating models. Horizontal resolution (°) of their atmospheric  
747    component models and convection schemes are also indicated.

748

749    Table 2. MJO simulation fidelity metrics derived from observations and participating  
750    models.

751

752    Table 3. Correlation coefficients between measures of the fidelity of MJO simulation.

753

## Figure list

Figure 1. Precipitation amount ( $\text{mm day}^{-1}$ ) corresponding to precipitation percentiles. Lower 70 percentiles are presented.

Figure 2. Same as Figure 1, except for upper 30 percentiles.

Figure 3. RHCP diagnostics created using ERA-I (a-c) and MERRA (d-e) relative humidity (%) and precipitations ( $\text{mm day}^{-1}$ ) from a, d) GPCP (1997-2008), b, e) TRMM (1998-2008), and c) ERA-I (1989-2008). f) Uncertainty of the observed RHCP diagnostic, estimated as the standard deviation of all five results divided by the average of them. Daily averaged precipitation and RH over the equatorial Indian Ocean ( $10^{\circ}\text{S}$ - $10^{\circ}\text{N}$ ,  $60$ - $90^{\circ}\text{E}$ ) are used to construct the RHCP diagnostic.

Figure 4. RHCP diagnostics at 850 hPa created using all participating models (color lines), and that with three different precipitation products combined with ERA-I RH (black lines). In the lower part of left panel, the method to calculate the moisture sensitivity metric is illustrated.

Figure 5. Same as Figure 4, except that the RHCP diagnostics are constructed using 700 hPa RH.

Figure 6. Correlation coefficients between the moisture sensitivity metric ( $\overline{RH}^{\text{upper } X\%} - \overline{RH}^{\text{lower } Y\%}$ ) and three MJO simulation fidelity metrics: a) E/W ratio, b) East power, and c)  $R_{\text{max}}$ . The correlation coefficients are displayed as a function of X and Y. d) Average of all results (a-c).

Figure 7. (left) Sensitivity of correlation coefficients between the moisture sensitivity metric ( $\overline{RH}^{\text{upper } X\%} - \overline{RH}^{\text{lower } Y\%}$ ) and three MJO simulation fidelity metrics to a) Y with X fixed as 10, and to b) X with Y fixed as 20. (right) Same as left panels, but percentage variance (%) of inter-model spread in MJO simulation fidelity metrics explained by the moisture sensitivity metric. Black solid line in each panel represents the average of correlation coefficients (left) or percentage variance (right) of all MJO simulation fidelity metrics.

Figure 8. Scatter plot between the moisture sensitivity metric ( $\overline{RH}^{\text{upper } X\%} - \overline{RH}^{\text{lower } Y\%}$ ) with X=10 and Y=20 and three MJO simulation fidelity metrics: a) E/W ratio, b) East power, and c)  $R_{\text{max}}$ . Open circles represent model simulations, while the observed values are indicated by closed triangles. The linear fit to the model data and

792 the percentage variance of the MJO simulation fidelity metrics explained by the RH  
793 metric and the linear relationship is also displayed in each panel.  
794

Table 1. List of participating models. Horizontal resolution (°) of their atmospheric component models and convection schemes are also indicated.

Model	Horizontal resolution (Atmos.)	Convection scheme
bccr_bcm2_0	1.9 x 1.9	Bougeault (1985)
cccma_cgcm3_1_t63	1.9 x 1.9	Zhang and McFarlane (1995)
cnrm_cm3	1.9 x 1.9	Bougeault (1985)
gfdl_cm2_0	2 x 2.5	Moorthi and Suarez (1992); Tokioaka et al. (1988)
gfdl_cm2_1	2 x 2.5	Moorthi and Suarez (1992); Tokioaka et al. (1988)
giss_aom	3 x 4	Del Genio and Yao (1993)
hadgem3	2.86 x 1.25	Gregory and Rowntree (1990)
iap_fgoals1_0_g	2.8 x 2.8	Zhang and McFarlane (1995)
ingv_echam4	1.1 x 1.1	Tiedtke (1989); Nordeng (1994)
inmcm3_0	4 x 5	Betts (1986)
miroc3_2_medres	2.8 x 2.8	Arakawa and Schubert (1974); Pan and Randall (1998); Emori et al. (2001)
miub_echo_g	3.9 x 3.9	Tiedtke (1989); Nordeng (1994)
mpi_echam5	1.9 x 1.9	Tiedtke (1989); Nordeng (1994)
mri_cgcm2_3_2a	2.8 x 2.8	Arakawa and Schubert (1974); Pan and Randall (1998); Emori et al. (2001)
BNU-ESM	2.8 x 2.8	Zhang and McFarlane (1995); Neale et al. (2008); Richter and Rasch (2008)
CanESM2	2.8 x 2.8	Zhang and McFarlane (1995)
CMCC-CM	0.75 x 0.75	Tiedtke (1989); Nordeng (1994)
CMCC-CMS	1.9 x 1.9	Tiedtke (1989); Nordeng (1994)
CNRM-CM5	1.4 x 1.4	Bougeault (1985)
FGOALS-s2	2.8 x 1.6	Tiedtke (1989); Nordeng (1994)
IPSL-CM5A-LR	3.75 x 1.8	Emanuel (1991)
MIROC4h	0.56 x 0.56	Arakawa and Schubert (1974); Pan and Randall (1998); Emori et al. (2001)
MIROC-ESM	2.8 x 2.8	Arakawa and Schubert (1974); Pan and Randall (1998); Emori et al. (2001)
MIROC-ESM-CHEM	2.8 x 2.8	Arakawa and Schubert (1974); Pan and Randall (1998); Emori et al. (2001)
MPI-ESM-LR	1.9 x 1.9	Tiedtke (1989); Nordeng (1994)

MPI-ESM-MR	1.9 x 1.9	Tiedtke (1989); Nordeng (1994)
MRI-CGCM3	1.1 x 1.1	Tiedtke (1989); Nordeng (1994); Yukimoto et al. (2011)
NorESM1-M	2.5 x 1.9	Zhang and McFarlane (1995); Neale et al. (2008); Richter and Rasch (2008)

798

799 Table 2. MJO simulation fidelity metrics derived from observations and participating  
800 models.  
801

Data	East/West	East	R <sub>max</sub>
GPCP/AVHRR	2.20	0.22	0.67
TRMM/AVHRR	2.73	0.20	0.67
ERA-I/AVHRR	2.09	0.10	0.67
bccr_bcm2_0	3.50	0.21	0.47
cccma_cgcm3_1_t63	1.29	0.06	0.3
cnrm_cm3	5.91	0.28	0.43
gfdl_cm2_0	2.58	0.15	0.52
gfdl_cm2_1	1.96	0.12	0.37
giss_aom	0.7	0.03	0.12
hadgem3	1.24	0.07	0.24
iap_fgoals1_0_g	0.9	0.03	0.15
ingv_echam4	1.03	0.07	0.33
inmcm3_0	0.63	0.04	-
miroc3_2_medres	1.68	0.08	0.33
miub_echo_g	1.89	0.25	0.59
mpi_echam5	1.85	0.22	0.4
mri_cgcm2_3_2a	1.38	0.07	0.46
BNU-ESM	1.6	0.09	0.34
CanESM2	0.87	0.03	0.04
CMCC-CM	3.05	0.27	0.61
CMCC-CMS	2.14	0.25	0.45
CNRM-CM5	4.95	0.46	0.67
FGOALS-s2	1.56	0.13	0.36
IPSL-CM5A-LR	1.59	0.06	0.26
MIROC4h	1.62	0.05	0.51
MIROC-ESM	0.91	0.04	0.24
MIROC-ESM-CHEM	0.65	0.04	0.16
MPI-ESM-LR	1.31	0.14	0.35
MPI-ESM-MR	1.62	0.19	0.35
MRI-CGCM3	3.15	0.25	0.56
NorESM1-M	2.64	0.15	0.51

802

Table 3. Correlation coefficients between measures of the fidelity of MJO simulation.

	East/West	East	R <sub>max</sub> <sup>†</sup>
East/West	1	0.83*	0.67*
East	-	1	0.74*
R <sub>max</sub>	-	-	1

\*: Statistically significant at 95% confidence level

†: inmcm3\_0 is missing OLR data.

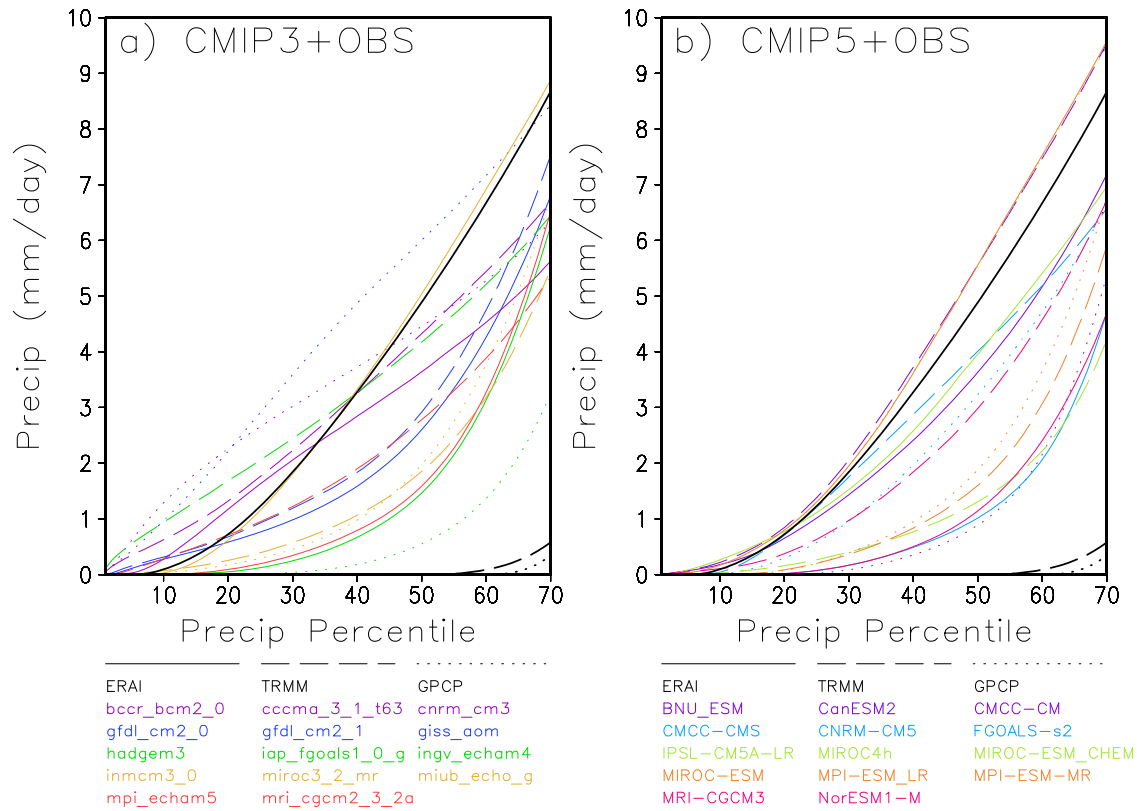


Figure 1. Precipitation amount ( $\text{mm day}^{-1}$ ) corresponding to precipitation percentiles over the equatorial Indian Ocean ( $10^{\circ}\text{S}$ - $10^{\circ}\text{N}$ ,  $60$ - $90^{\circ}\text{E}$ ). Lower 70 percentiles are presented.



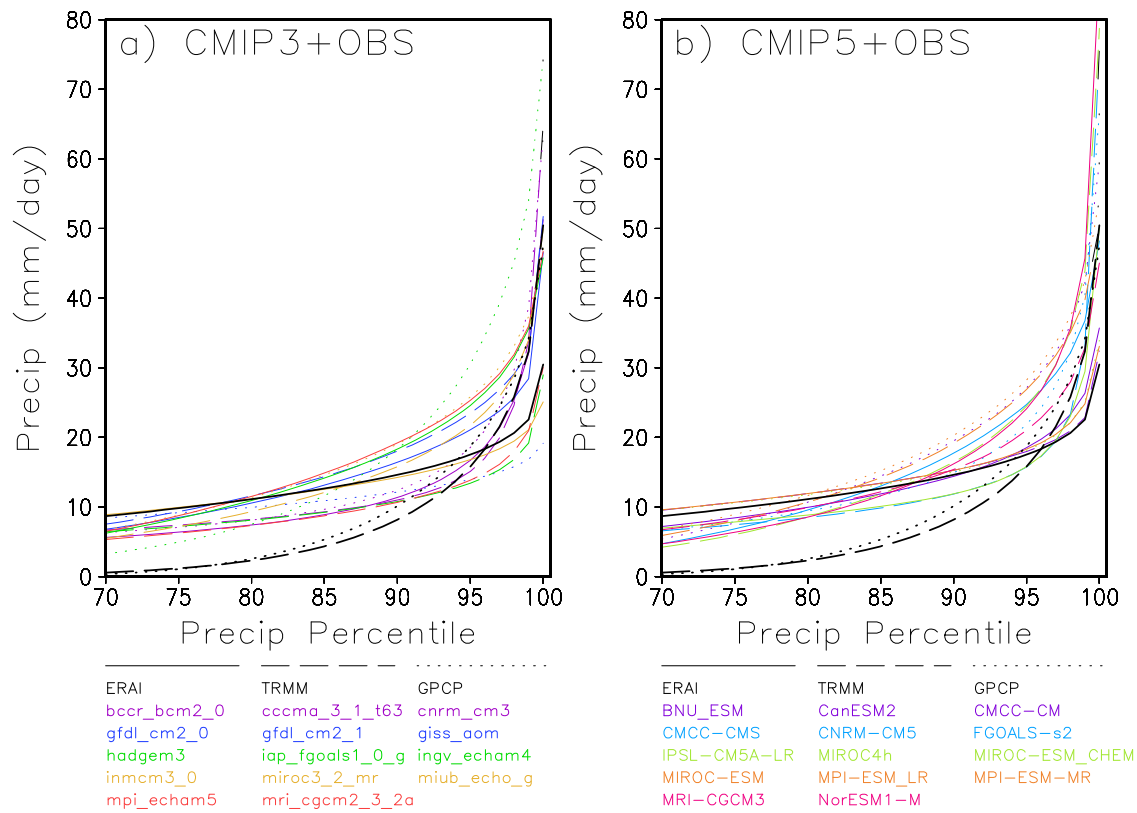


Figure 2. Same as Figure 1, except for upper 30 percentiles.

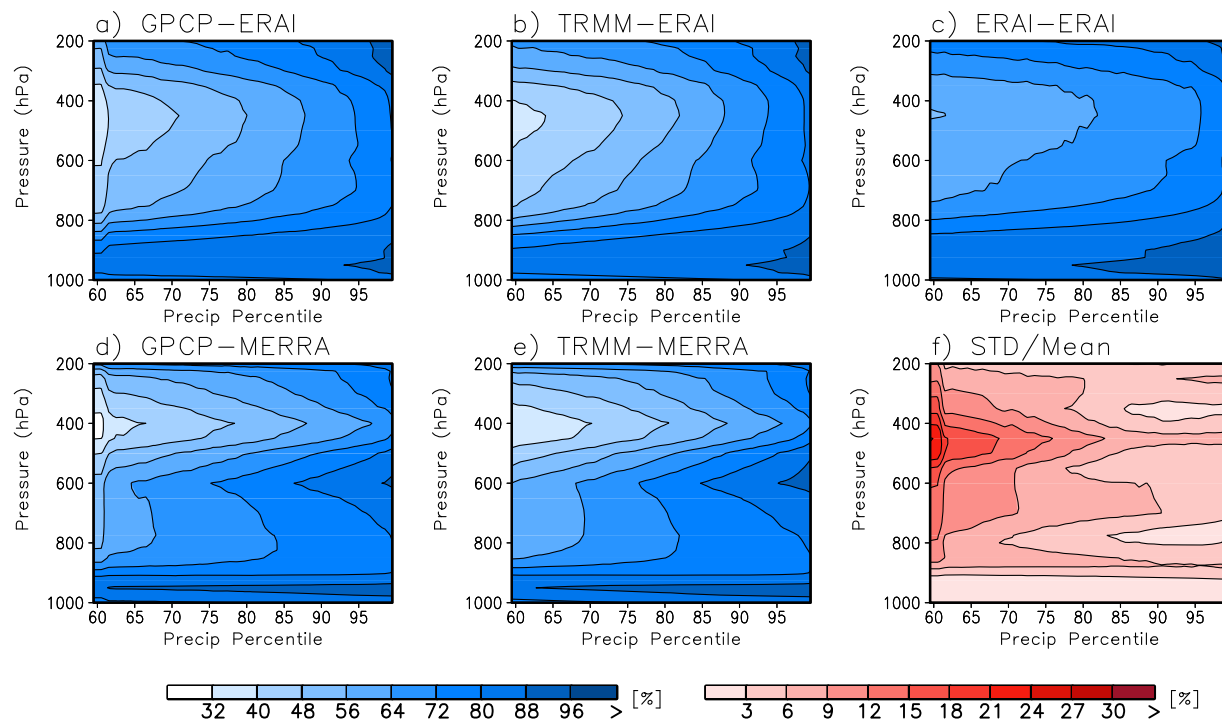


Figure 3. RHCP diagnostics created using ERA-I (a-c) and MERRA (d-e) relative humidity (%) and precipitations ( $\text{mm day}^{-1}$ ) from a, d) GPCP (1997-2008), b, e) TRMM (1998-2008), and c) ERA-I (1989-2008). f) Uncertainty of the observed RHCP diagnostic, estimated as the standard deviation of all five results divided by the average of them. Daily averaged precipitation and RH over the equatorial Indian Ocean ( $10^{\circ}\text{S}$ - $10^{\circ}\text{N}$ ,  $60$ - $90^{\circ}\text{E}$ ) are used to construct the RHCP diagnostic.

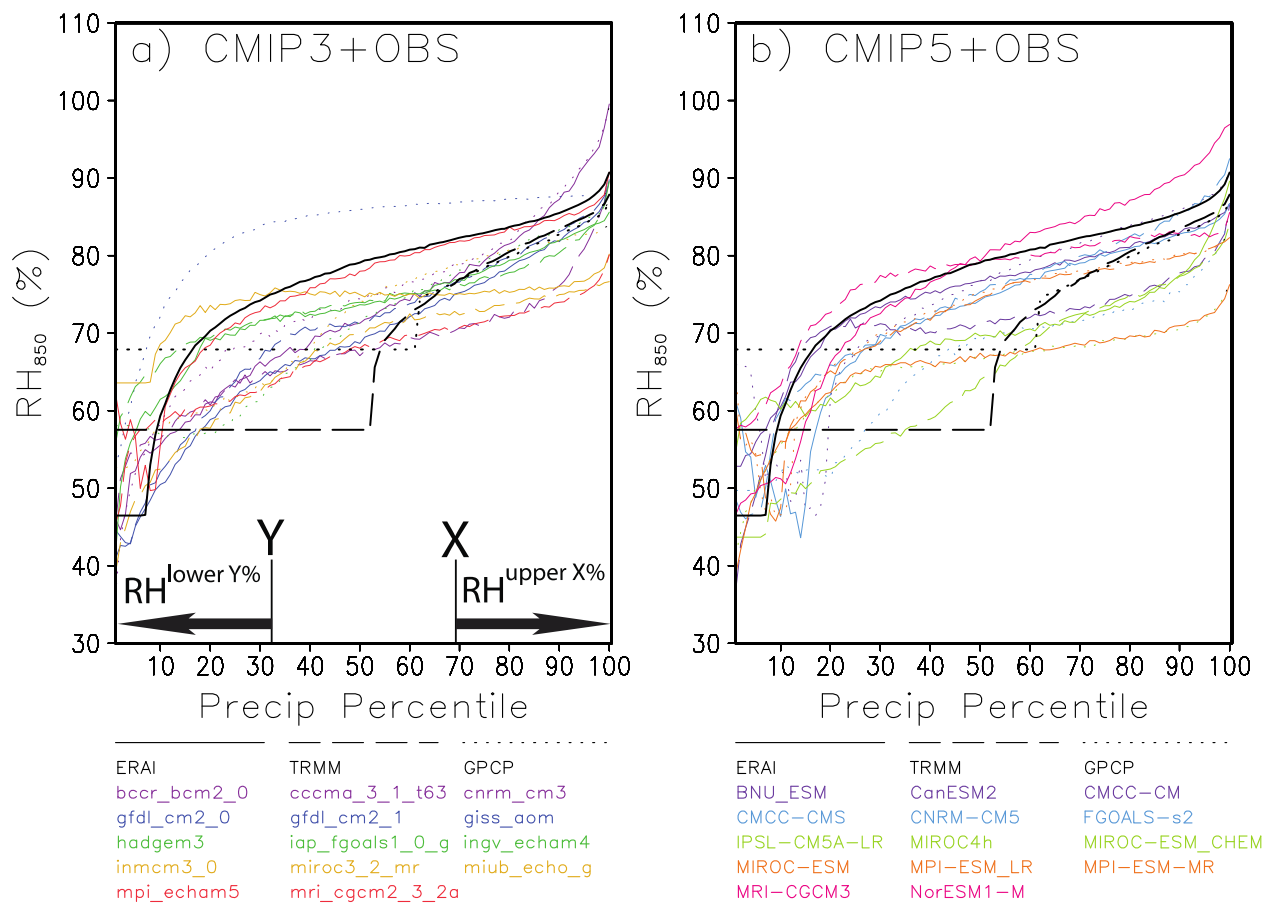


Figure 4. RHCP diagnostics at 850 hPa created using all participating models (color lines), and that with three different precipitation products combined with ERA-I RH (black lines). In the lower part of left panel, the method to calculate the moisture sensitivity metric is illustrated.

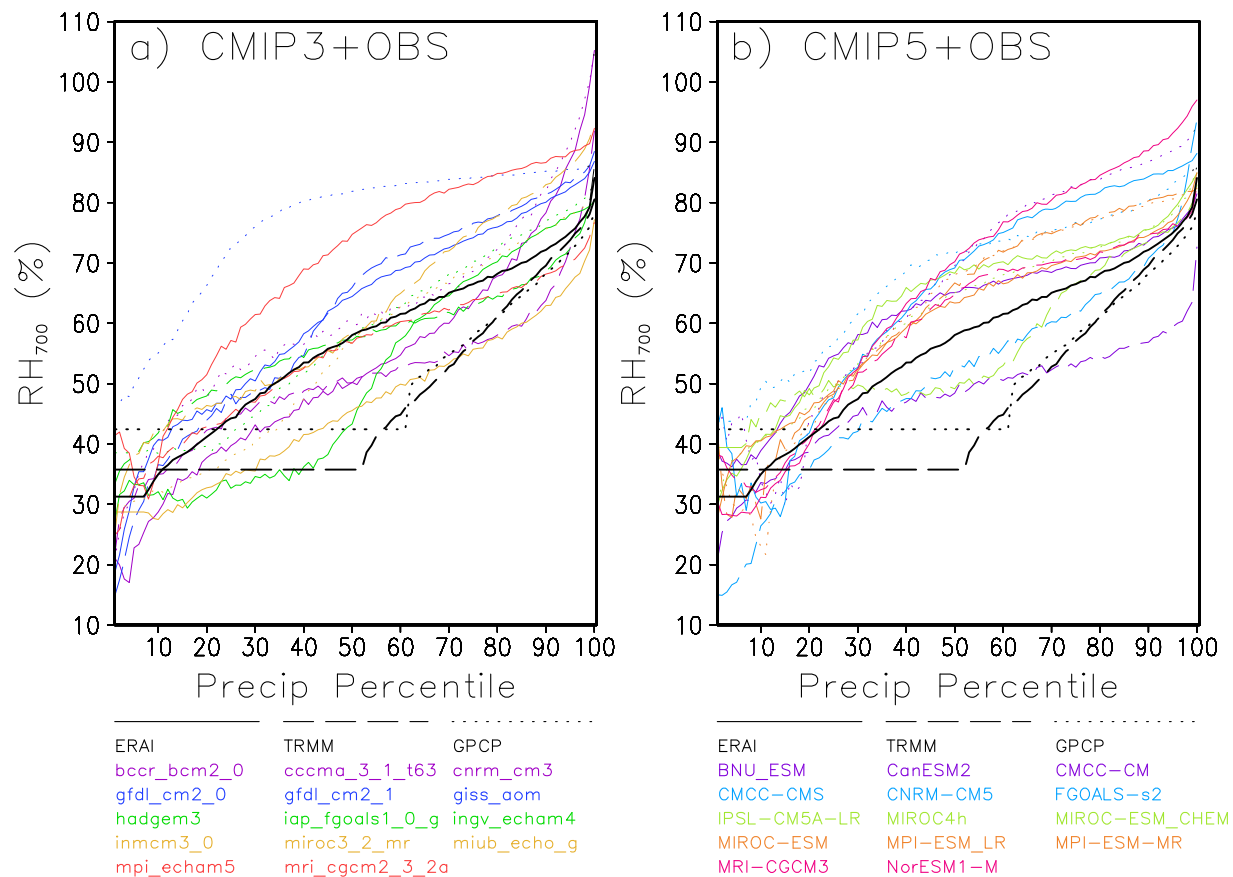


Figure 5. Same as Figure 4, except that the RHCP diagnostics are constructed using 700 hPa RH.

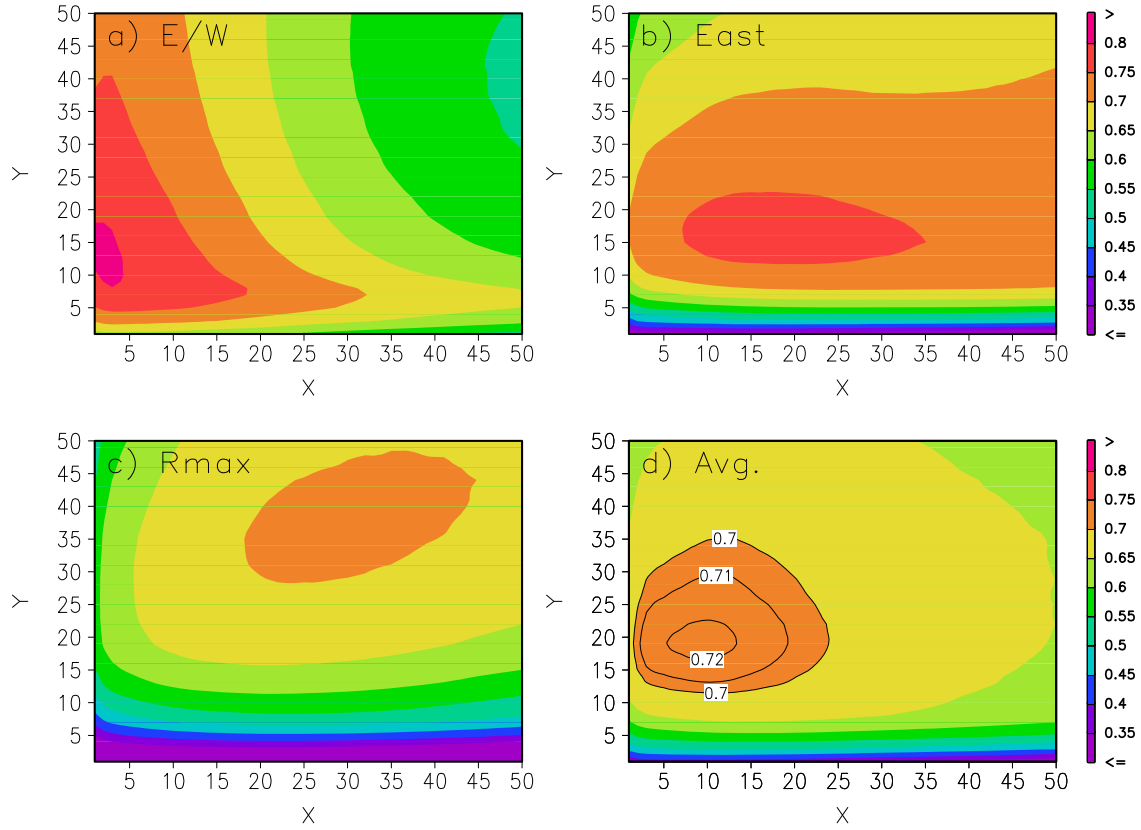


Figure 6. Correlation coefficients between the moisture sensitivity metric ( $\overline{RH}^{upper\ X\%} - \overline{RH}^{lower\ Y\%}$ ) and three MJO simulation fidelity metrics: a) E/W ratio, b) East power, and c)  $R_{max}$ . The correlation coefficients are displayed as a function of X and Y. d) Average of all results (a-c).

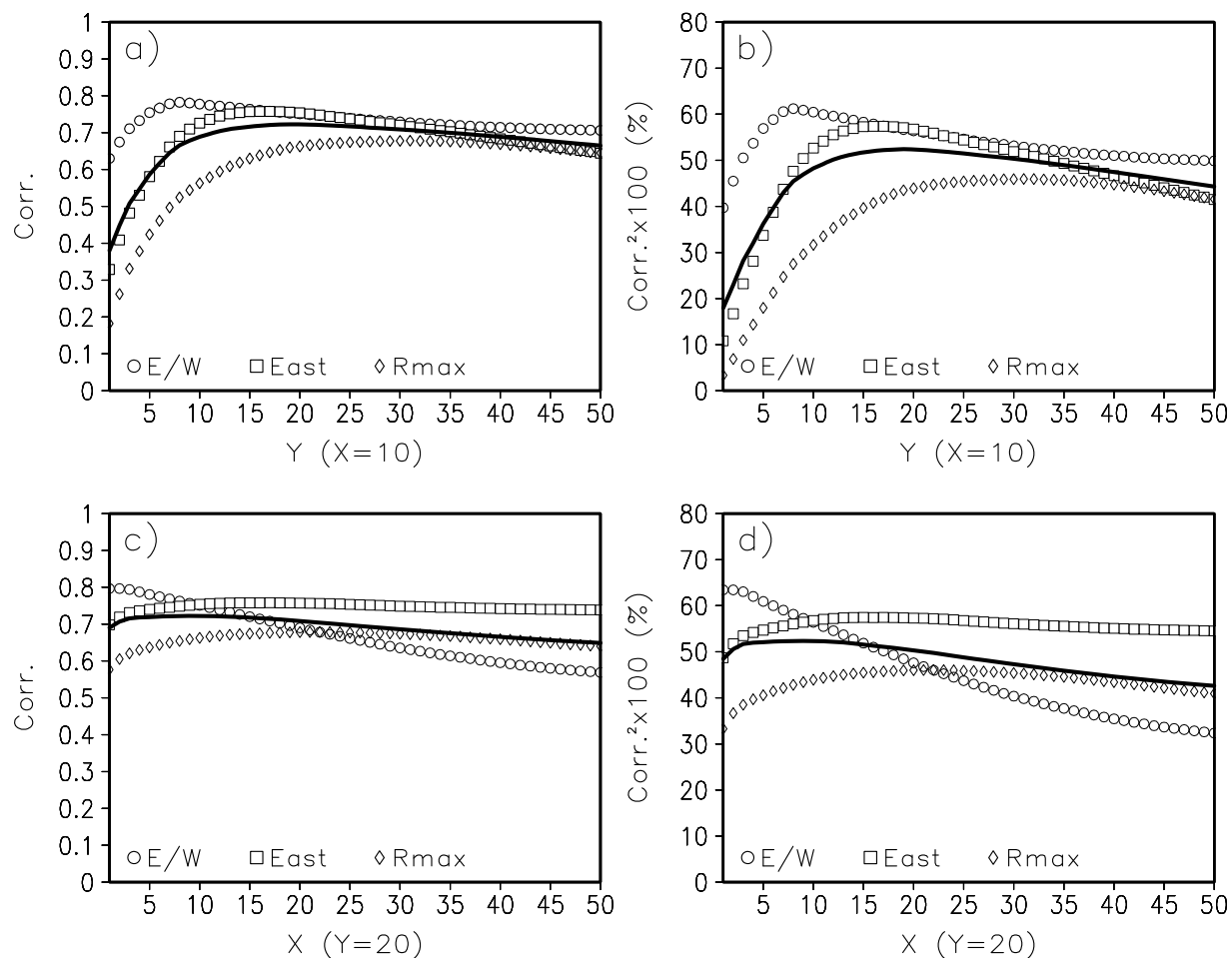


Figure 7. (left) Sensitivity of correlation coefficients between the moisture sensitivity metric ( $\overline{RH}^{upper X\%} - \overline{RH}^{lower Y\%}$ ) and three MJO simulation fidelity metrics to a) Y with X fixed as 10, and to b) X with Y fixed as 20. (right) Same as left panels, but percentage variance (%) of inter-model spread in MJO simulation fidelity metrics explained by the moisture sensitivity metric. Black solid line in each panel represents the average of correlation coefficients (left) or percentage variance (right) of all MJO simulation fidelity metrics.

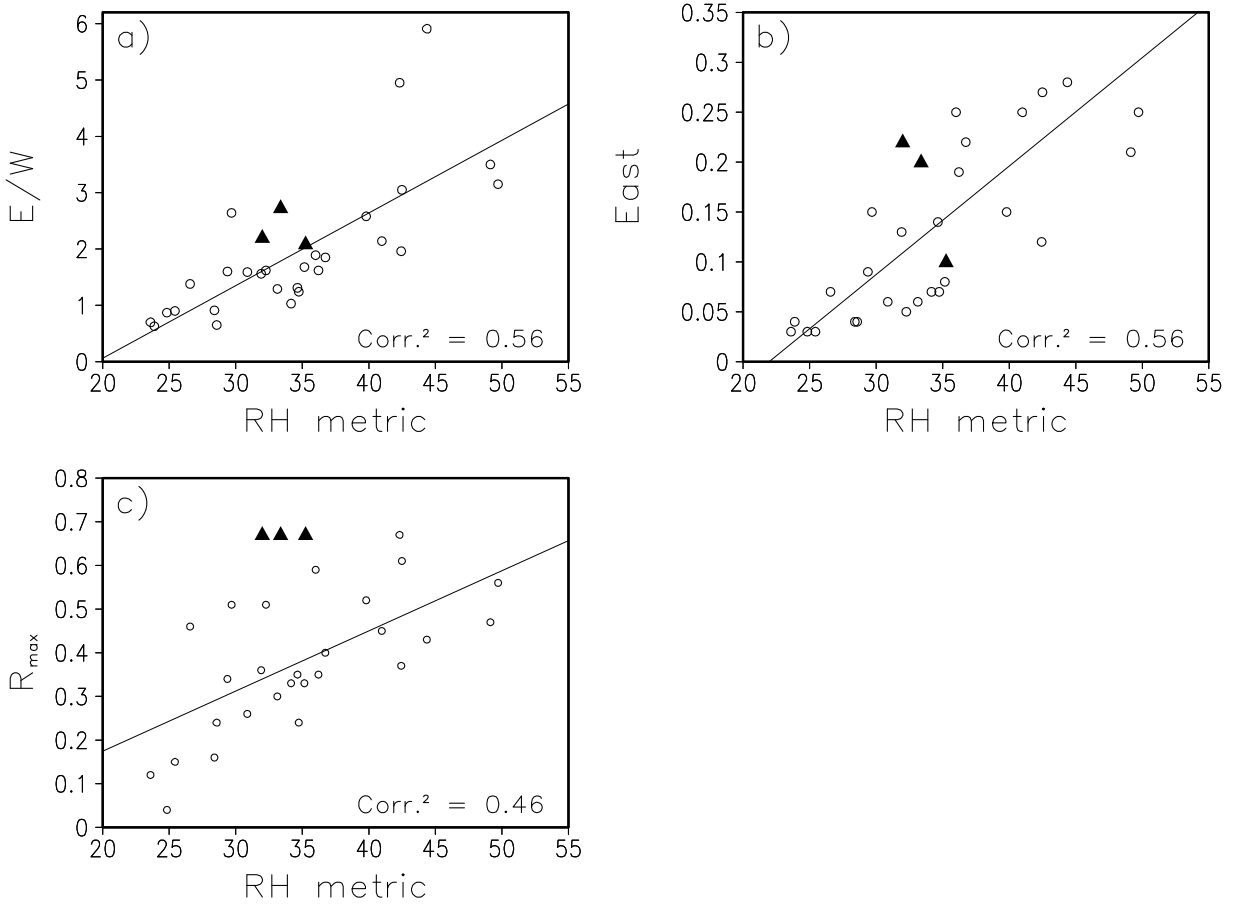


Figure 8. Scatter plot between the moisture sensitivity metric ( $\overline{RH}^{upper\ X\%} - \overline{RH}^{lower\ Y\%}$ ) with  $X=10$  and  $Y=20$  and three MJO simulation fidelity metrics: a)  $E/W$  ratio, b) East power, and c)  $R_{\text{max}}$ . Open circles represent model simulations, while the observed values are indicated by closed triangles. The linear fit to the model data and the percentage variance of the MJO simulation fidelity metrics explained by the RH metric and the linear relationship is also displayed in each panel.